Studies of the Effects of Optical System Errors on the HCIT Contrast Performance

Erkin Sidick*, Stuart Shaklan, Amir Give'on, and Brian Kern
Jet Propulsion Laboratory, California Institute of Technology, 4800 Oak Grove Drive, Pasadena, CA, USA 91109

ABSTRACT

The High Contrast Imaging Testbed (HCIT) at the Jet Propulsion Laboratory employs a broadband wavefront correction algorithm called Electric Field Conjugation (EFC) to obtain the required 10^{-10} contrast. This algorithm works with one deformable mirror (DM) to estimate the electric-field to be controlled, and with one or multiple DM's to create a "dark-hole" in a predefined region of the image plane where terrestrial planets would be found. We have investigated the effects of DM actuator errors and the optic position errors on the efficiency of the EFC algorithm in a Lyot coronagraph configuration. The structural design of the optical system as well as the parameters of various optical elements used in the analysis are drawn from those of the HCIT system that have been implemented with one DM. The simulation takes into account the surface errors of various optical elements. Results of some of these studies have been verified by actual measurements.

Key words: Coronagraphy, adaptive optics, space telescopes, exoplanets

1. INTRODUCTION

High-contrast imaging testbed (HCIT) at JPL is Terrestrial Planet Finder (TPF) Coronagraph's primary platform for experimentation [1-3]. It is used to provide laboratory validation of key technologies as well as demonstration of a flight-traceable approach to implementation. It employs a broadband wavefront correction algorithm called Electric Field Conjugation (EFC) to obtain the required 10^{-10} contrast [4]. This algorithm works with one or multiple deformable mirrors (DM's) to create a "dark-hole" in a predefined region of the image plane where terrestrial planets would be found. It achieves the desired high contrast level in two stages. The first is the reconstruction (or estimation) stage. In this stage, the algorithm provides an estimate of the aberrated complex electric field (e-field) in the image plane based on pairs of images taken at the final image plane using different DM configurations. The second is the correction or EFC stage. In this stage the algorithm generates a correction based on e- field estimated in the first stage. The correction is then applied to the DM actuators to null the image e-field in the predefined dark-hole region.

We have investigated the effects of DM actuator errors and the optic position errors on the efficiency of the EFC algorithm in a Lyot coronagraph configuration. Considered cases include dead actuators, lateral and longitudinal movement of the occulting mask, and the lateral movement of a flat optical surface. The structural design of the optical system as well as the parameters of various optical elements used in the analysis are drawn from those of the HCIT system that have been implemented with one DM. The simulation takes into account the surface errors of various optics. The optical simulation algorithm uses MACOS (Modeling and Analysis for Controlled Optical Systems) as its analytic tool [5]. Hence it is capable of performing full three-dimensional near-field diffraction analysis on HCIT's optical model. Results of some of these studies have been verified by actual measurements.

2. BACKROUND

2.1 The HCIT Optical System

The schematic diagram of the HCIT layout in the *xz*-plane is shown in Figure 1. Artificial starlight is created by a 5μm pinhole illuminated by an optical fiber. We assume a broadband light source centered at λ_0=800nm and having a bandwidth of ±10%, or $\Delta\lambda$=160nm. An off-axis parabolic mirror (OAP1) collimates the light from the pinhole and

*Erkin.Sidick@jpl.nasa.gov; Phone 1 818 393-7585; Fax 1 818 393-9471; www.jpl.nasa.gov

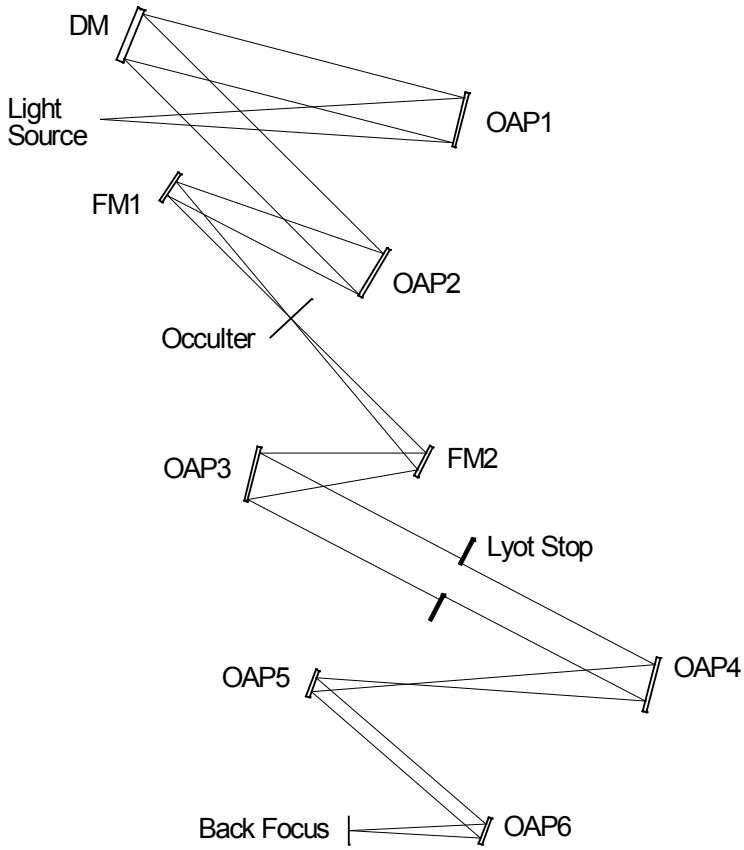

Figure 1. Schematic diagram of the High Contrast Imaging Testbed layout. The light source ("starlight") is a 5μm pinhole illuminated by an optical fiber, and a CCD science camera is located at the back focal plane for detecting the image of the "starlight".

directs it to a high-density, 32x32 actuator deformable mirror (DM), which performs wavefront control. A circular aperture mask on the DM defines the system pupil of the HCIT, and has a diameter of D=30mm. After the DM, the collimated light is re-imaged onto the focal plane of the occulting mask by OAP2 and a flat-mirror (FM1). The occulting mask attenuates the starlight, and almost has no effect on the light of a planet if present. The "back-end" of the system, from the occulting mask to the back focus plane, supports experimentation with diverse coronagraph configurations and apodizations. A flat mirror (FM2) and OAP3 re-collimate the light passing through the occulter mask and form a same-size sharp image of the DM pupil at the Lyot plane. A Lyot stop blocks the ring-like residual light diffracted off the occulting mask while letting most of the planet light through. After OAP4 forms an image from the remaining stellar and planet lights, it is then magnified (M ≈3) by the OAP5-OAP6 pair for proper sampling on the CCD science camera located at the back focal plane. More information on the HCIT and the DM can be found in Refs. [1-3].

2.2 Occulting Mask

In this paper, we use a linear-sinc^2 occulting mask consisting of platinum (Pt) deposited on a fused-silica and compensated with spatially profiled polymethyl methacrylate (PMMA) [6-8]. It has a linear-sinc^2 intensity profile with a one-dimensional transmittance profile $T(x)$ given by:

$$T(x) = \left[1 - \left(\frac{\sin(\pi x / w)}{(\pi x / w)} \right)^2 \right]^2 . \tag{1}$$

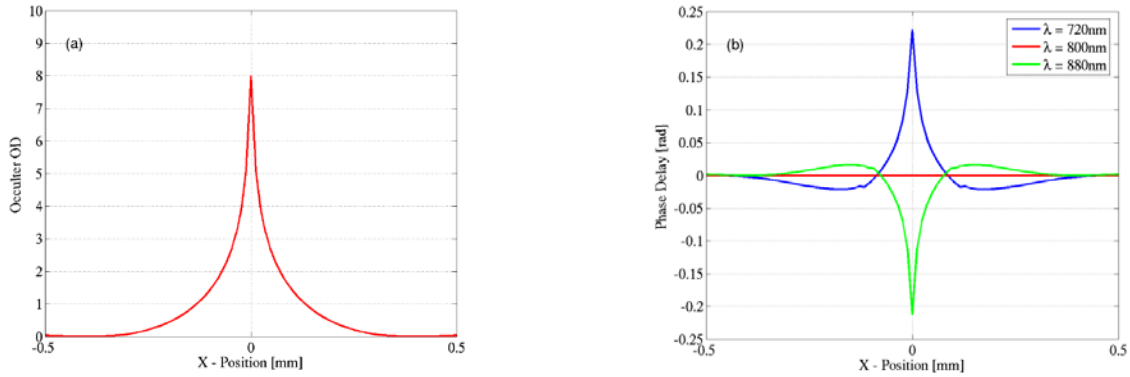

Figure 2. (a) Optical density (OD) and (b) phase profiles of a linear-sinc^2 occulting mask consisting of platinum (Pt) deposited on a fused-silica and compensated with spatially profiled PMMA.

This mask has a constant (zero) phase at λ_0=800nm, but its phase is non-zero and varies with both the optical density (OD) of the occulter and the wavelength, λ. Figures 2(a) shows the OD profile of the occulter as a function of the *x*-position. The dependence of the OD on λ is negligibly small, therefore, it is ignored in this paper. But we include the dispersion of the occulter phase in our simulations. The profiles of the occulter phase at three different wavelengths are shown in Fig. 2(b). The width of this occulter is $w = 144\mu\text{m}$, which gives $T(x) = 0.5$ at $x/f = 4\lambda/D$, where $D = 30\text{mm}$ is the diameter of the system clear aperture. The front end F-number (F/#) of this optical system is 25.8.

2.3 Other Optical Components

The DM used on the HCIT has 1024 (32x32) actuators arrayed on a 1mm pitch. Its description is given in detail in Ref. [1], and will not be repeated here.

Our Lyot stop is a simple blackened piece of sheet metal with a sharp edge. Its opening (Lyot stop aperture) has an eye-shape defined by two circles that are shifted with respect to each other in the horizontal direction by a distance of ε in units of *D*. The value of ε needs to be chosen based on the value of the occulting mask width parameter *w*, and ε=0.36 in this paper.

In our simulations, we include the surface errors of six OAP's and two FM's shown in Figs. 4(a-h) of Ref. [3]. Some optics on the current HCIT have surface height errors different from the above, and we used them here just to introduce some realistic surface errors into the HCIT optical model.

2.4 Definitions of Half Dark-Hole Area and Contrast

For the current optical system with only one DM, we carry out wavefront control (WFC) over a region Ω_c, where Ω_c is a D-shaped half dark-hole region bound by $x/f = X \geq 4\lambda/D$ and $\sqrt{x^2+y^2}/f = R = 11\lambda/D$, or $[X, R] = [5, 11]\lambda/D$. We will evaluate the performance of the HCIT using either the normalized intensity,

$$I(x,y) = I_o(x,y)/I_{uo\max}, \tag{2}$$

or the contrast,

$$C(x,y) = I(x,y)[T_0/T(x,y)] = [I_o(x,y)/I_{uo\max}][T_0/T(x,y)], \tag{3}$$

where $I_o(x,y)$ is the image intensity of the occulted star, $I_{uo\max}$ is the maximum value of the unocculted star intensity, $T(x,y)$ is the occulter transmittance, and T_0 is the maximum value of the $T(x,y)$. We will keep track of the following three contrast parameters in this paper: (i) C_b, the mean contrast inside a "Big" D-shaped region Ω_b defined by $[X, R] = [5, 10]\lambda/D$. (ii) C_s, the mean contrast inside a "Small" square region Ω_s from $X = 4\lambda/D$ to $5\lambda/D$ and from $y/f = Y = -0.5\lambda/D$ to $0.5\lambda/D$. (iii) C_m, the "Maximum" contrast value inside the small square region Ω_s. Similarly, we use I_b, I_s and I_m to denote the big-region mean, the small-region mean, and the small-region maximum of the

normalized intensity. The nominal contrast values obtained for a narrowband light with $\lambda_0 = 800\text{nm}$ and the error-free optical system without conducting any wavefront control are $C_b = 2.54\text{E}-14$, $C_s = 1.32\text{E}-13$, and $C_m = 2.93\text{E}-13$, respectively. When the phase errors of the eight optics are included in simulation, the above intensity values change to $C_b = 3.98\text{E}-6$, $C_s = 4.88\text{E}-5$, and $C_m = 8.41\text{E}-5$, respectively.

2.5 About the Wavefront Control (WFC) Algorithm

In this paper, we use a control algorithm similar to the "minimum-wavefront and optimal control compensator" described in detail in Ref. [9]. This approach is also called "Actuator regularization" [4]. The WFC algorithm described in Ref. [9] uses the wavefront at the system exit pupil as its input, and calculate the actuator commands as its output. In the present case we set the DM actuators to superpose the negative of the e-field onto the image plane, with a goal to make the image intensity zero on the region Ω_c on the image plane. Therefore, the WFC algorithm uses an e-field column-vector $\vec{\mathbf{e}}$ as its input, where

$$\vec{\mathbf{e}} = \begin{bmatrix} \Re(\vec{\mathbf{E}}) \\ \Im(\vec{\mathbf{E}}) \end{bmatrix}. \tag{4}$$

The joint cost function now becomes as

$$J = \frac{1}{2}\left(\vec{\mathbf{e}}^T\vec{\mathbf{e}} + \gamma_{\text{wu}}\vec{\mathbf{u}}^T\vec{\mathbf{u}}\right), \tag{5}$$

and the gain matrix $\widetilde{\mathbf{G}}$ is obtained from

$$\widetilde{\mathbf{G}} = \left[\widetilde{\mathbf{S}}^T\widetilde{\mathbf{S}} + \gamma_{\text{wu}}\widetilde{\mathbf{I}}\right]^{-1}\widetilde{\mathbf{S}}^T. \tag{6}$$

In Eq. (4), $\vec{\mathbf{E}}$ is the column-vector of the complex e-field on region Ω_c. It is normalized by the maximum value of the reference e-field, the one obtained when no one actuator is actuated, and is formed by stacking the elements of the complex e-field on region Ω_c in a certain order, as was explained in Eq. (1) of Ref. [9]. The $\Re(\vec{\mathbf{E}})$ and the $\Im(\vec{\mathbf{E}})$ are the real and the imaginary parts of $\vec{\mathbf{E}}$, respectively. In Eq. (6), the $\widetilde{\mathbf{S}}$ is the sensitivity matrix consisting of the influence functions of all actuators. The MACOS simulation tool calculates the complex e-field at the final focal plane directly. Therefore, the e-field estimation step is actually not needed in our simulation. However, we will use this step when we evaluate the effects of DM actuator errors for they will have an impact on both the e-field estimation and control processes. The simulation creates a 512x512-pixel image plane, with ~5 pixels per $f\lambda/D$. Considering only the pixels in the dark hole gives an e-field vector, $\vec{\mathbf{e}}$, having a size of 6032x1 pixels. There are a total of 1024 DM actuators in the current 1-DM system, but we exclude the actuators with zero or very weak influences, thus reducing the number of the actuators used to 932.

3. SIMULATION RESULTS

We now describe our simulation results on the effects of dead actuators, lateral and longitudinal movement of the occulting mask, and the lateral movement of a flat optical surface on the contrast performance of the HCIT. We start with the nominal case where only the optical surface errors and the occulter phase are included in the simulation.

3.1 Nominal Case

We use the EFC-based broadband wavefront correction algorithm described Ref. [4] in our simulations. The broadband sensitivity-matrix $\widetilde{\mathbf{S}}$ consists of five monochromatic sensitivity matrices corresponding to wavelengths λ_1=720nm, λ_2=760nm, λ_3=800nm, λ_4=840nm, and λ_1=880nm, respectively. That is, we carry out the WFC at those five wevelengths simultaneously. We calculate the broad-band contrast in the following way: Divide the full bandwidth $\Delta\lambda$=160nm into 4 equal segments with a wavelength increment of $\delta\lambda$=40nm, representing the $\Delta\lambda$=160nm broad-band light with 5 narrow-band (or monochromatic) beams with equal intensity centered at the above five wavelengths. We calculate the final image plane intensity maps at each of these wavelengths separately, rescale them to the pixel size the same as that of $\lambda_3 = \lambda_0$ = 800nm beam, and average them to obtain the broad-band image intensity map. We perform

this calculation on the occulted and the unocculted images separately to obtain their broadband images first, then use these averaged images to obtain a broadband contrast map.

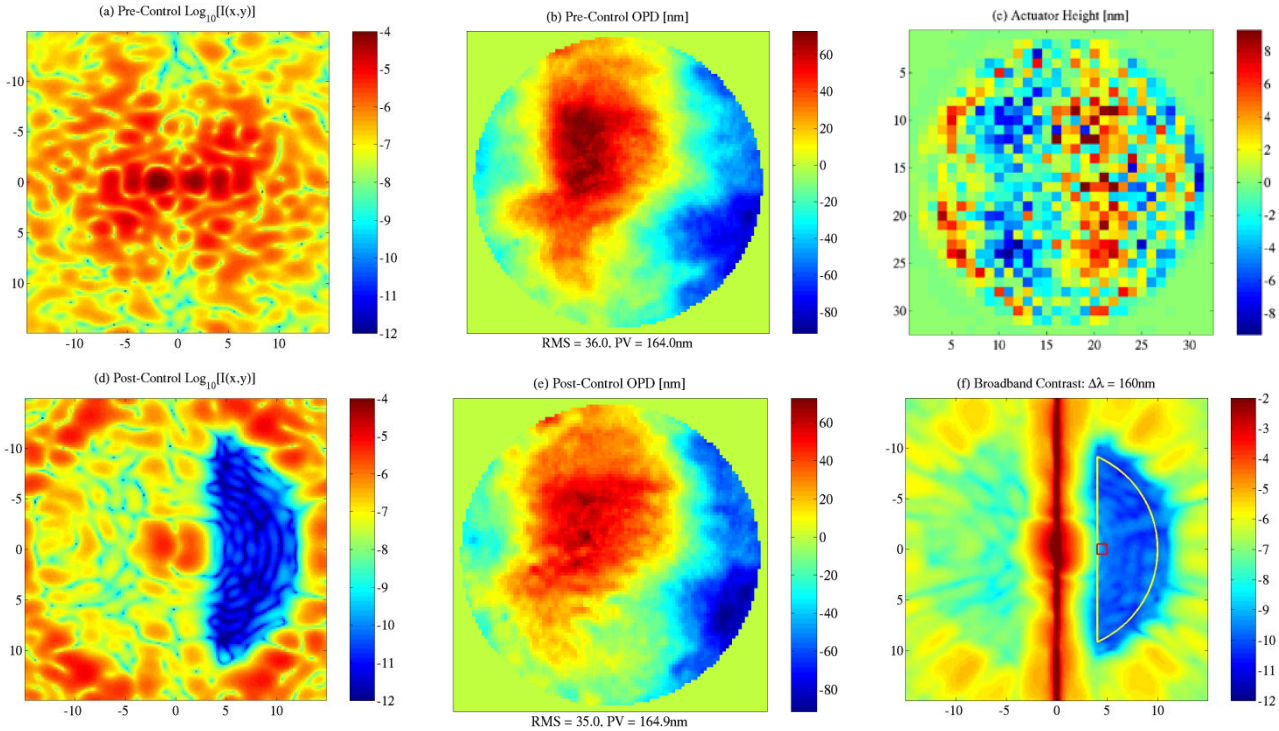

Figure 3. (a) Log-scale PSF before WFC when $\lambda_3 = \lambda_0 = 800$nm, where the units of the horizontal- and the vertical-axes are λ/D. (b) Exit-pupil Optical Path Difference (OPD) before WFC. (c) Actuator-height map obtained at the end of broadband WFC, where the units of the horizontal- and the vertical-axes are mm. (d)-(e) PSF and OPD when $\lambda_3 = \lambda_0 =$ 800nm, and the broadband contrast obtained at the end of broadband WFC. The yellow- and the red-lines in part (f) show the boundaries of the regions in which C_b, C_s and C_m are defined. In parts (b) and (e), the "RMS" and the "PV" denote the root-mean-square and the peak-to-valley values of the OPD.

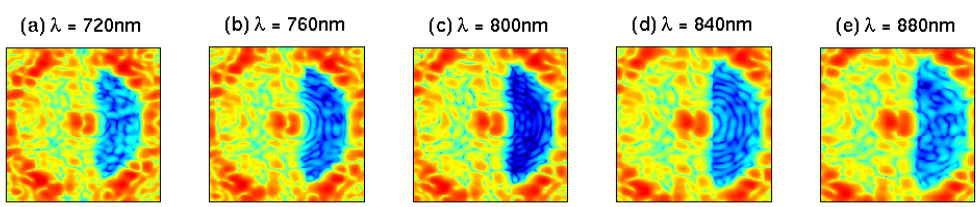

Figure 4. $\text{Log}_{10}[I(x,y)]$ at five different wavelengths. The ranges of the horizontal- and the vertical axes are from -15λ/D to +15λ/D, and the stretch of all the color maps is -12 to -4.

When we include the surface errors of the eight optical surfaces and the occulter phase only, we obtain the $I(x,y)$ and the exit-pupil Optical Path Difference (OPD) as shown in Figs. 3(a-b) at $\lambda_3 = \lambda_0 = 800$nm before WFC. After conducting broadband WFC for 25 iterations, we obtain a DM solution as shown in Fig. 3(c), the $I(x,y)$ and the OPD maps as shown in Figs. 3(d-e), and a broadband contrast map as in Fig. 3(e). The corresponding $I(x,y)$ maps at the five wavelengths are shown in Fig. 4. The three contrast values corresponding to Fig. 3(e) are $C_b = 1.85\text{E}-10$, $C_s = 9.92\text{E}-10$, and $C_m = 3.20\text{E}-9$, respectively. As has been shown before, the WFC (or the EFC) process does not minimize the wavefront error at the exit-pupil, instead re-arranges it to create a dark-hole in the pre-determined region. These results are included here as a baseline to the simulations to be presented in the following sub-sections.

In the above WFC simulation, we used an optimized set of two actuator regularization values, $\gamma_{wu} = [50\ 100]/\text{nm}^2$, with the corresponding WFC iteration numbers listed in the same order, $N_{WFC} = [15\ 10]$. That is, the WFC process is completed in two phases with two different γ_{wu} values in the order given above, each with a different WFC iteration number also given above. We didn't use the e-field estimation routine in the current nominal case, instead obtained the complex e-field directly from our MACOS simulation tool. However, we will use the e-field estimation routine whenever the errors introduced have an impact on the process of e-field estimation.

It should be mentioned that the sensitivity matrix $\tilde{\mathbf{S}}$ is obtained for this nominal case, where the initial e-field at $\lambda = \lambda_0 =$ 800nm corresponds to the intensity map shown in Fig. 3(a). Also, the same sensitivity matrix $\tilde{\mathbf{S}}$ is used in all control iterations, that is, the $\tilde{\mathbf{S}}$ is not updated or altered during a WFC process, and the same $\tilde{\mathbf{S}}$ of the current nominal case is used in all other non-nominal cases.

3.2 Dead Actuators

Actuator errors affect both the e-field estimation and control [10]. Therefore, we will obtain the complex e-field on the final image plane using the e-field estimation routine described in Ref. [4]. The four probe DM settings used in our e-field estimation calculation are obtained with $\theta = 0$, $\pi/2$, π and $3\pi/2$, respectively. The DM height maps of the first two settings are shown in Figs. 5(a-b) for P = 5nm.

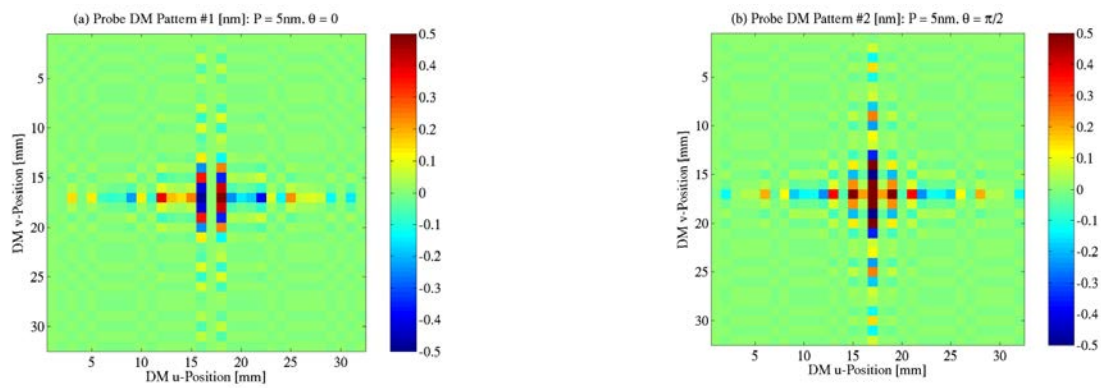

Figure 5. Actuator height maps of two probe DM settings with (a) $\theta = 0$ and (b) $\theta = \pi/2$, respectively. The other two settings have $\theta = \pi$ and $3\pi/2$, and are not shown here.

The first error we examined is the case where two actuators on row v = 17mm and are separated by 2mm (or interleaved by one actuator) are not responsive to the applied commands, and remain fixed at the mid-point of their control range. We call such actuators "dead actuators" in this paper. In the current simulations, for the optical system with all eight phase errors, we obtained probe actuator command patterns as usual, but set the command values of the selected actuators to 0nm (the mid-point of the -200nm to 200nm range) when performing each e-field estimation calculation. We did the same to the actuator command solutions obtained in each WFC iteration: The sensitivity matrix $\tilde{\mathbf{S}}$ is kept the same, but the command values of the dead actuators are set to 0nm. The dead actuators selected are shown on the map of actuator positions in Fig. 6(a), where each of the different pairs of the dead-actuators are marked with the same color and the same shape. When there is no dead-actuator in the system, we obtain I_b as a function of control iteration number and wavelength as shown in Fig. 6(b). It displays the efficiency of e-field estimation and control achieved at the end of each control iteration. Figure 6(c) shows the similar result when the two actuators on columns u = 9,11mm are dead. As compared to the case of Fig. 6(b), the contrast performance becomes worse in this case as expected. Figure 6(d) compares the values of $I_b(\lambda$=800nm) of all the cases considered. As expected, the final value of $I_b(\lambda$=800nm) moves higher as the dead-actuators move closer to the DM center, but the process of e-field estimation and control does not completely fail in any case considered. That is, this simulation predicts that if any two actuators separated by 2mm die, the process of e-field estimation and control either does not get affected or lose some efficiency, but still yields acceptable contrast values.

Next, we investigated the cases where three actuators separated by 2mm (interleaved by one actuator) are dead. Figure 7(a) compares the values of $I_b(\lambda$=800nm) for six groups of dead actuators on row v = 17mm. As we can see, the e-field

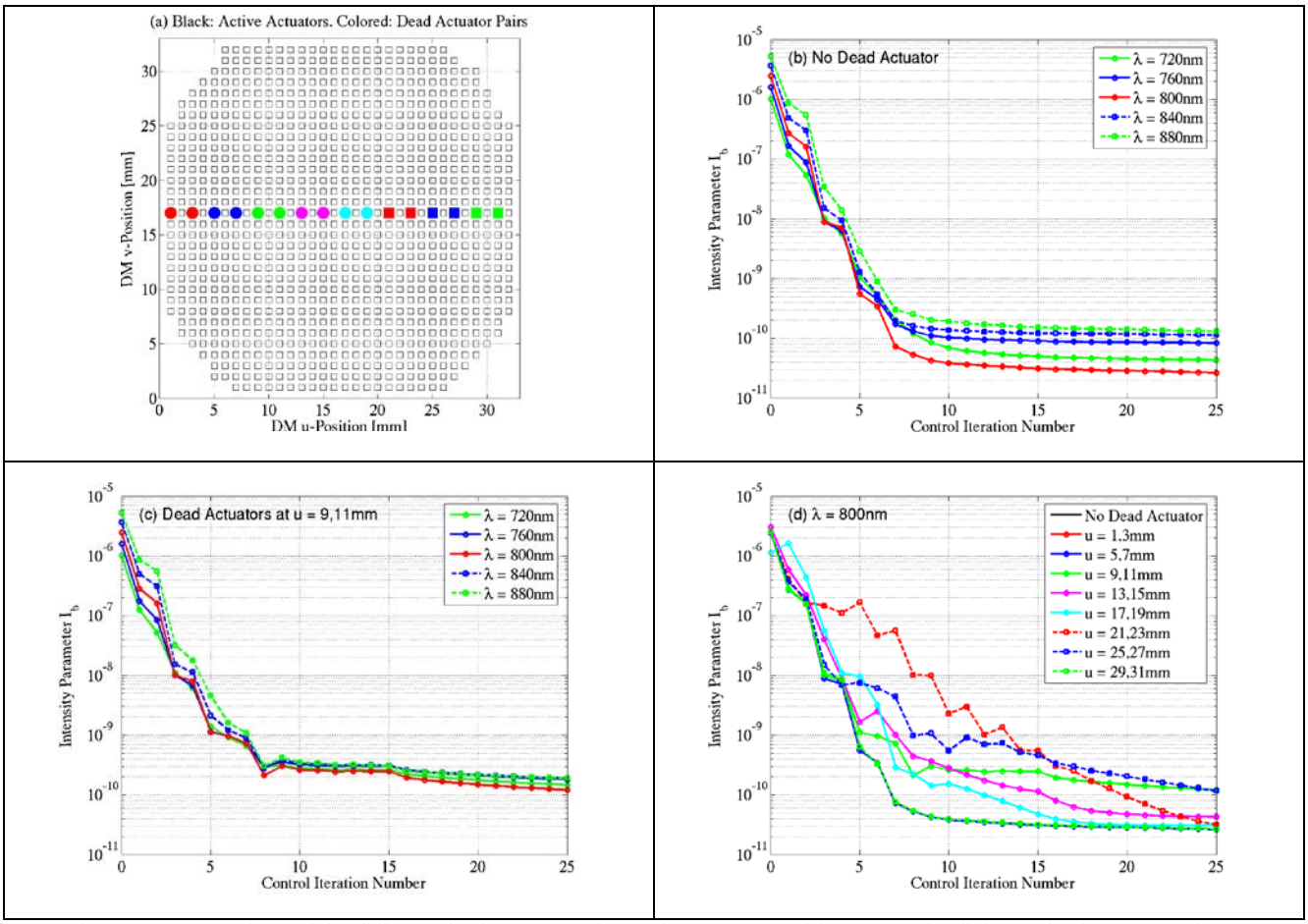

Figure 6. (a) Locations of the different dead actuator pairs on the actuator position map. The different dead actuator pairs are marked with the different colors and/or the different shapes. (b) I_b versus control iteration number when there is no any dead actuator. (c) I_b versus control iteration number when the two actuators at u = 9,11mm are dead. (d) Comparison of I_b(λ=800nm) versus control iteration number curves obtained for different pairs of dead actuators whose u-positions are indicated in the figure legend.

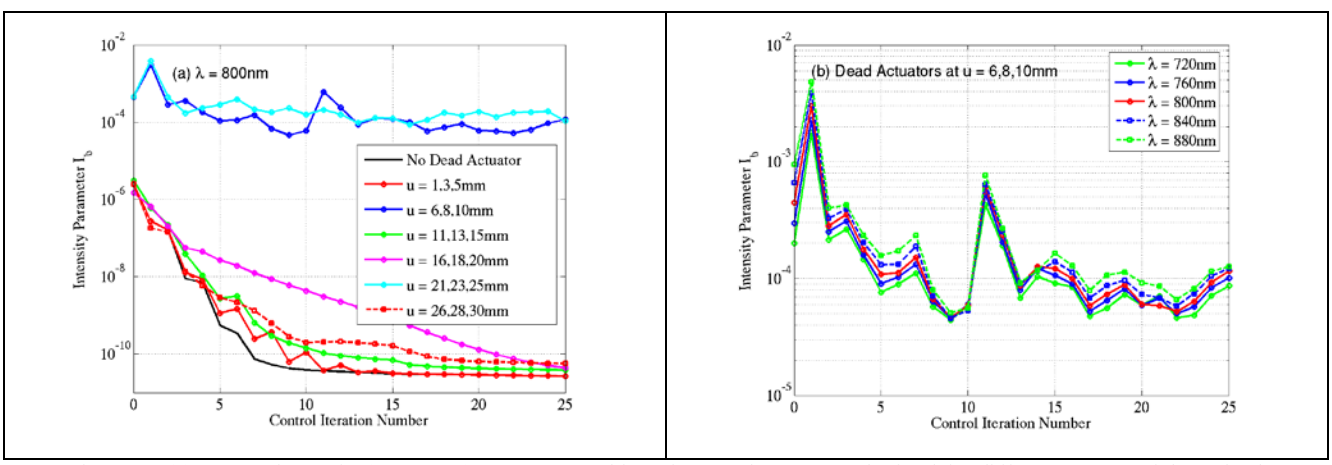

Figure 7. (a) Comparison of I_b(λ=800nm) versus control iteration number curves obtained for different groups of three dead actuators on row v = 17mm and on u-positions indicated in the figure legend. (b) I_b versus control iteration number when the three actuators at u = 6,8,10mm are dead.

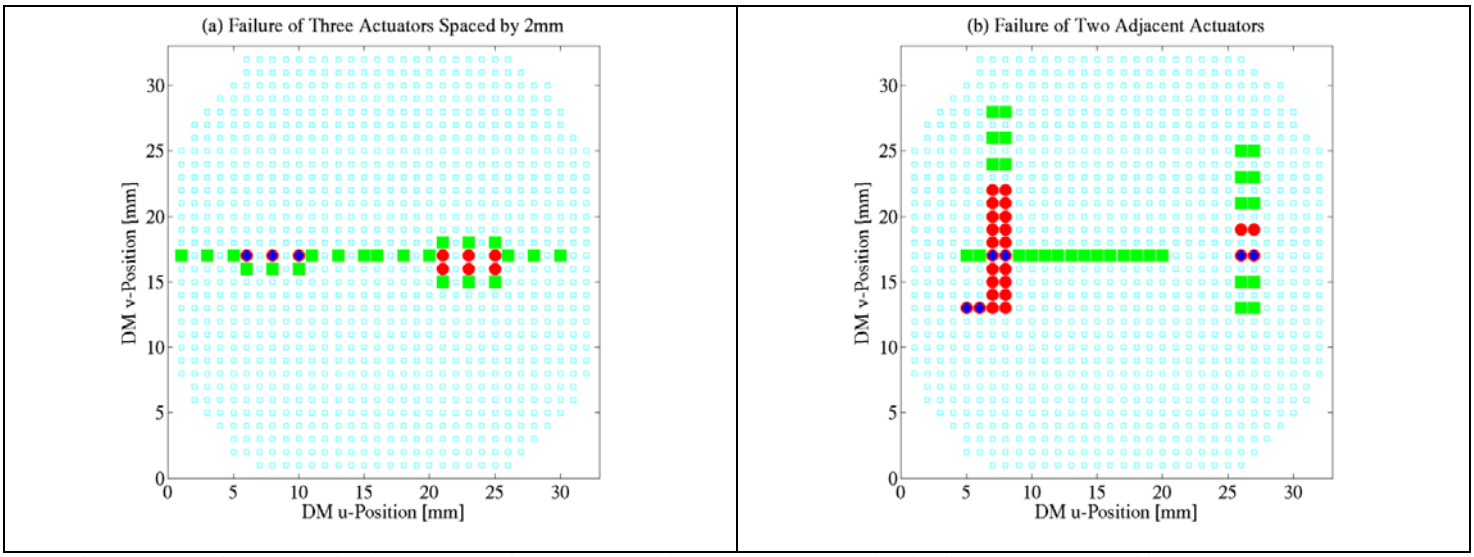

Figure 8. Locations of the dead actuators on the actuator position map. (a) Cases of 3-dead-actuators separated by 2mm (interleaved by one actuator), and (b) cases of 2-adjacent actuators dead. The green-color indicates the dead-actuators groups that work, the red-color indicates the groups that fail, and the blue-color on top of the read-color indicates the group which fails when conducting e-field estimation but works without it.

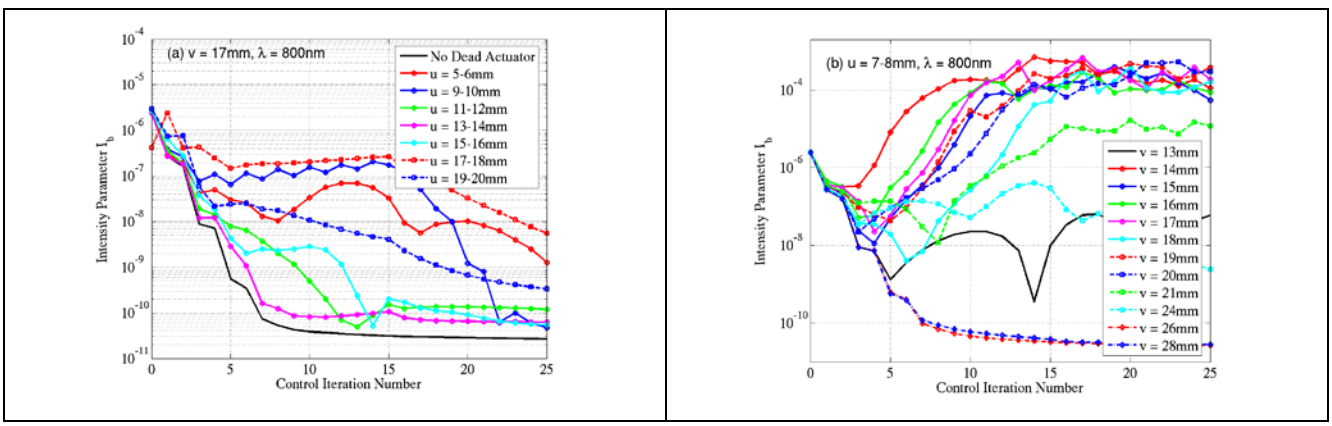

Figure 9. Comparison of $I_b(\lambda$=800nm) versus control iteration number curves obtained for the cases of two adjacent actuators dead. (a) For actuators on row v = 17mm and on u-positions indicated in the figure legend. (b) For actuators on columns u = 7,8mm and on v-positions indicated in the figure legend.

estimation and control processes do not fail in all cases except those where the dead actuators are located at u = 6,8,10mm and u = 21,23,25mm, respectively. The I_b of the case where the dead actuators are located at u = 6,8,10mm is shown as a function of control iteration number and the wavelength in Fig. 7(b). We have also examined several other dead actuator groups located on rows v = 15, 16 and 18mm. For the case where the dead actuators are located at v = 17mm and u = 6,8,10mm, we tested our WFC algorithm without performing e-field estimation, that is, by obtaining the e-field from our MACOS simulation tool directly, and found that the WFC process still works in this case. That is, the failure of this case is caused by the failure of the e-field estimation process, not by the WFC process. The "pass/fail" results of all the investigated cases with three dead actuators are shown on the actuator position map of Fig. 8(a), where the green-color indicates the 3-dead-actuators groups that work, the red- color indicates the groups that fail, and the blue-color on top of the read-color indicates the group which fails when conducting e-field estimation but works without it.

The last actuator errors we investigated are the cases where two adjacent actuators are dead at a time. The locations of the actuators considered are shown in Fig. 8(b), where the meanings of the different actuator colors are the same as in Fig. 8(a). We found that the e-field estimation and control processes are much more sensitive to the dead actuators located on two columns u = 7-8mm and are on or close to row v = 17mm than the other pairs considered. Again, three

pairs of actuators that originally failed worked fine when not using the e-field estimation process. Figure 9(a) compares the I_b(λ=800nm) versus control iteration number curves of the cases where v = 17mm (the result of the case where u = 7-8mm is shown in part (b)), and Fig. 9(b) compares the same for the dead actuator pairs located on columns u = 7-8mm.

In Ref. [10], we also investigated the effects of one, two or three randomly selected dead actuators on the four-probe e-field estimation and the EFC-based WFC performance of the High Contrast Imaging Testbed Phase Induced Amplitude Apodization (HCIT/PIAA) coronagraph system at JPL. It was shown that the effect of the one, two or three dead actuators, at least for the most cases considered there, is to slow down the process of WFC. The majority of realizations gave acceptable contrast values below 10^{-9} in 50 WFC iterations.

Although we haven't conducted an exhaustive search on the number and the distribution of the dead actuators that can be tolerated, the above results show that the HCIT Lyot coronagraph system is fairly robust for the 1-3 dead actuators. Even when 1-3 "critical" actuators is or are dead, we still have the option to rotate the DM, move the DM, or move the probe DM patterns such that those dead actuators no longer become critical. This is one of the significant findings of this study.

3.3 Lateral Translation of a Flat Optic

In order to estimate the sensitivity of the HCIT's monochromatic contrast on the lateral movement of a flat optic, we translated FM1 along the x-axis by T_x after WFC, and evaluated the changes in the normalized intensity parameters. In Fig. 1, positive T_x moves the FM1 into the paper (and towards the dark-hole). In this part of our simulations, we didn't use the e-field estimation algorithm because the errors introduced (x-translation of FM1) do not affect the process of e-field estimation. If we introduce a sinusoidal surface error into FM1 as shown in Fig. 10(a) and "turn off" all of the other surface errors, carry out WFC to create a dark-hole for a monochromatic beam with λ = 800nm and T_x = 0, and finally find the changes in normalized intensity parameters, $\Delta I(x,y)$, as a function of FM1- T_x, we obtain the curves in Fig. 10(b). In this figure, the "True (solid)" and the "Predicted (dashed)" results were obtained from

$$\begin{aligned} &\text{True}: \ \Delta I(x,y) = \left|E(x-T_x,y)-E(x,y)\right|^2 / I_{uo\max} \\ &\text{Predicted}: \ \Delta I(x,y) = (\pi/\lambda)^2[PV(\Delta OPD)/2]^2\left|M(x-N_x\lambda f/D,y)E(x',y')\right|^2 / I_{uo\max} \end{aligned} \quad . \tag{7}$$

where $E(x,y)$ is the complex e-field, $PV(\Delta OPD)$ is the Peak-to-Valley value of the change in the exit-pupil OPD, $\Delta OPD = OPD(T_x) - OPD(0)$, $M(x,y)$ is the complex transmission coefficient of the occulting mask, and N_x is the spatial-frequency of the sinusoidal surface error of the FM1 in cyc/aper. The origin of the (x,y) coordinate frame is at $(N_x\lambda f/D, 0)$, and that of the (x',y') frame is at (0,0). In Fig.10(b), the root-mean-square (RMS), the average (Mean), and the maximum (Max) values of $\Delta I(x,y)$ are evaluated over a square region having a width of $a = 1f\lambda/D$. As we can see from Fig. 10(b), the "True" and the "Predicted" values of the $\Delta I(x,y)$ parameters agree well in this case.

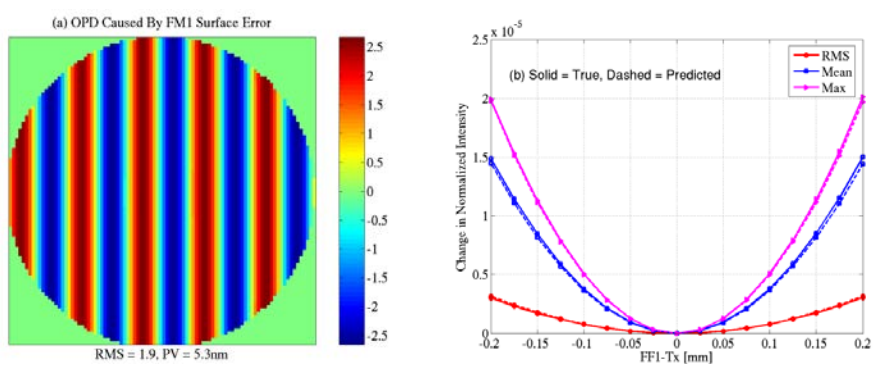

Figure 10. (a) Exit-pupil OPD caused by a sinusoidal surface error of FM1. (b) Change in normalized intensity parameters, root-mean-square (RMS), average (Mean), and maximum (Max), as a function of FM1- T_x.

We also investigated the case where the surface error of FM1 is not sinusoidal. When the "true" surface error of only the FM1 used in the previous sub-sections is included in our model, we obtain an exit-pupil OPD map as shown in Fig. 11(a). If we include the surface errors of all eight optics, the $OPD(0)$ becomes the same as shown in Fig. 3(b). When T_x

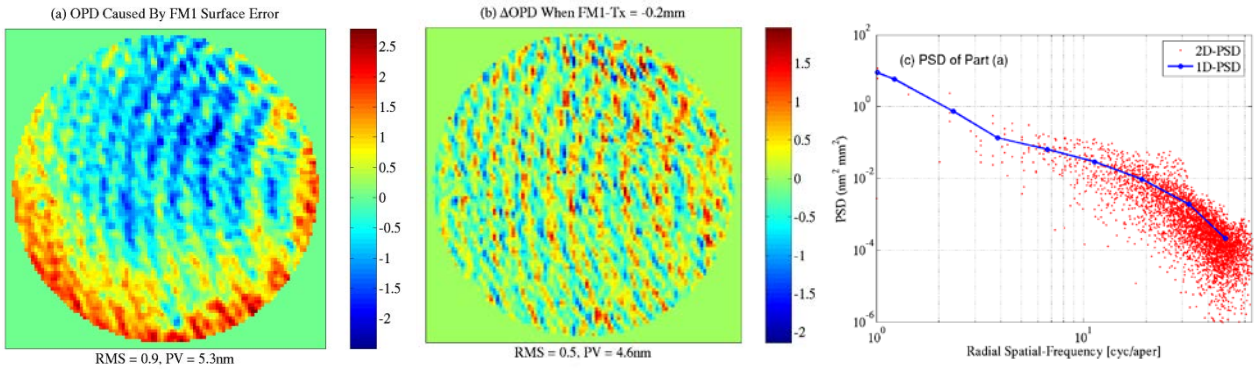

Figure 11. (a) Exit-pupil OPD caused by the FM1 "true" surface error only. (b) Change in exit-pupil OPD when FM1 is translated by T_x = -0.2mm. (c) Two-dimensional (2D) PSD of the OPD in part (a) and its radially-averaged 1-D version versus radial spatial-frequency.

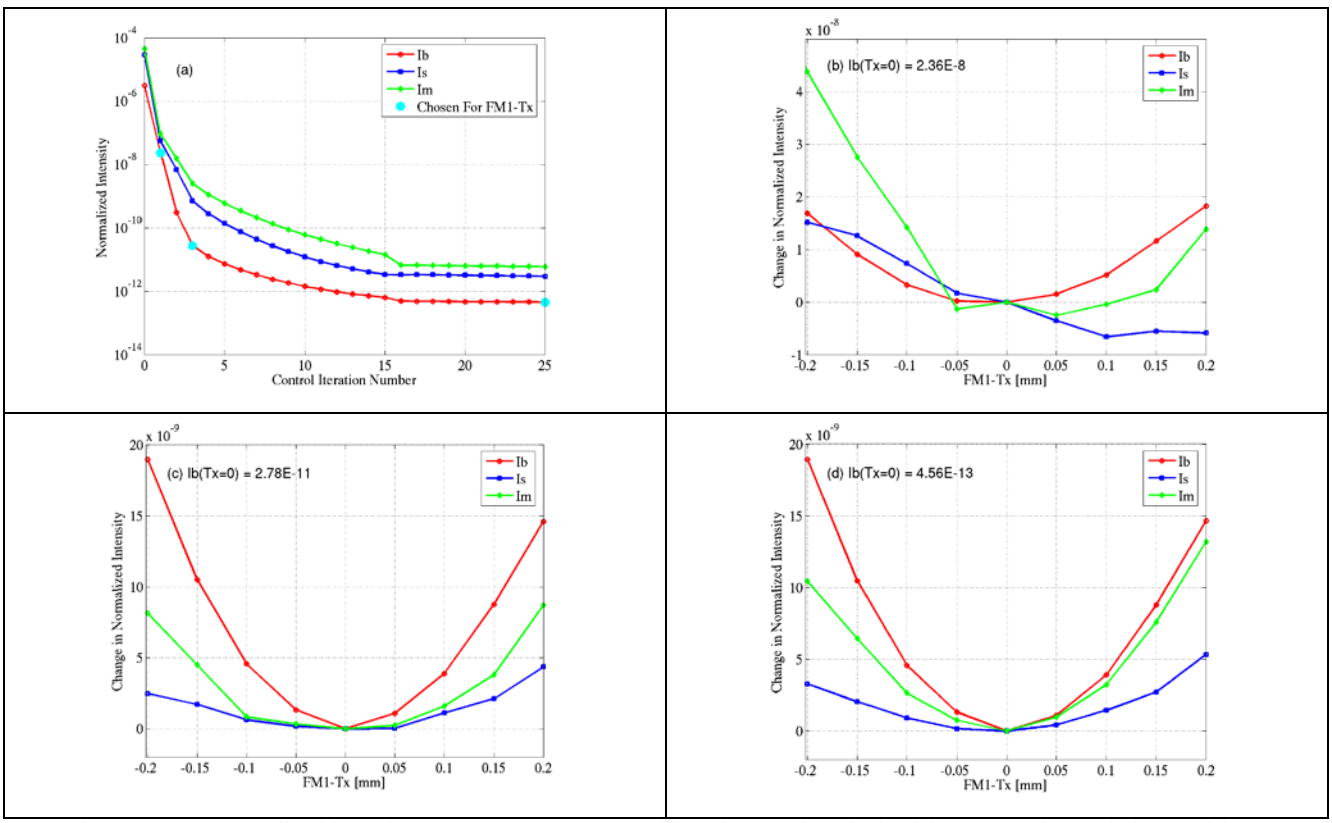

Figure 12. (a) Normalized intensity parameters versus control iteration number obtained for a monochromatic beam with λ=800nm. The surface errors of all eight optics are included in the simulation. (b)-(d) Variation of the normalized intensity parameters as a function of FM1- T_x (translation of FM1 along the x-axis) corresponding to three different contrast levels. The value of I_b when T_x = 0 is given as an insert along with the figure number.

= -0.2mm, we obtain a ΔOPD map as shown in Fig. 11(b), and its PSD as shown in Fig. 11(c), where the blue-curve is the 1-D (one-dimensional) version of the 2D-PSD calculated using the method described in Ref. [11]. For this case, we first carried out WFC for T_x = 0, and obtained the normalized intensity versus control iteration number result as shown in Fig. 12(a). Then, for the three different contrast levels shown by the cyan-color filled circles in Fig. 12(a), we calculated the changes in the values of the three normalized intensity parameters, I_b, I_s, and I_m, as a function of FM1- T_x, and obtained the results shown in Figs. 12(b-d). As we can see, none of the I_i –curves, where $i = b$, s or m, is symmetric with

respect to T_x , and they become more irregular when the darkness of the dark-hole reduces. Also, the sensitivity of contrast to FM1- T_x becomes stronger when the darkness of the dark-hole achieved is weaker. For this case, we found it difficult to do exact predictions as in the case of FM1 sinusoidal surface error shown in Fig. 10(b). This is because in the current case a spatial-frequency component of the ΔOPD is not well defined and $\Delta I(x,y)$ in the vicinity of $(N_x \lambda f / D, 0)$ is the combined product of all the spatial-frequency components of the ΔODP.

3.4 Translation of Occulter along the x- and z-Directions

We conducted an experiment on the HCIT to measure the sensitivity of narrow-band contrast on the *x*- (de-centering, T_x) and the *z*- (de-focusing, T_z) translations of the occulter. We carried out simulations on the same situation to find out how well the model predictions match with the experimental findings. The HCIT setup used for this experiment is slightly different from what was described in Section 2. That is, in this setup, $D = 48\text{mm}$, $\varepsilon = 0.4$, the front end F/# = 31.25, and the occulter is a thin-film Ni occulter deposited on a glass. This occulter has an OD-dependent phase profile similar to the blue-curve in Fig. 2(b) with a peak value of ~1.2 radians at the operating wavelength of λ = 800nm. We matched our optical model to this HCIT setup by using the same OD- and phase-profiles (designed, not measured) for the occulter while adjusting its width so that $T(x) = 0.5$ at $x / f = 3.3\lambda / D$, the same as on the testbed. No attempt has been made to match the magnitude and the registration of the optical surface errors between the experimental setup and the model—The same surface errors of the eight optics used in the simulations of the previous sub-sections were used for this simulation.

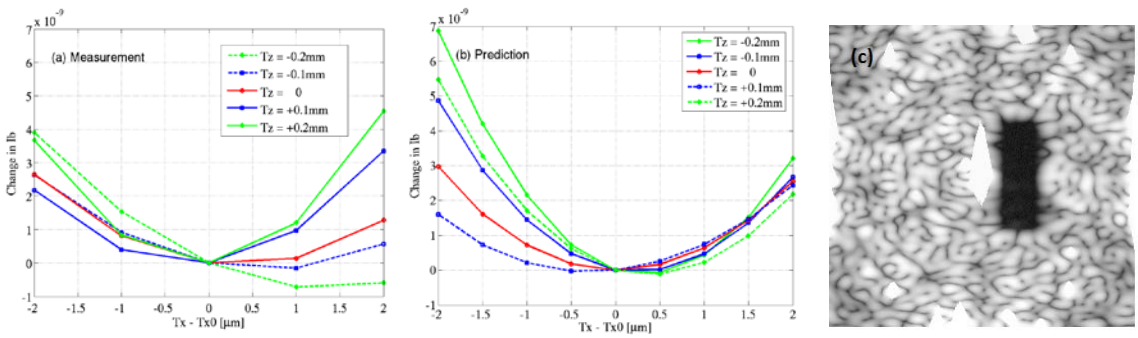

Figure 13. Sensitivity of I_b to occulter T_x and T_z. (a) Measured, and (b) simulated. (c) Normalized intensity map measured when $T_x = T_z = 0$, where $I_b = 2.91\text{E-}9$.

In the experiment, a rectangle-shaped half dark-hole was first created with the occulter at its nominal position ($T_x = T_z = 0$) in two WFC steps. In the first step, the exit-pupil wavefront was minimized through a normal, wavefront-based control procedure. In the next step, a dark-hole was created using the EFC-based correction procedure. Then the occulter T_x - and T_z -sensitivities of the contrast were measured with the following steps: (1) Move the occulter by T_z = -0.2mm (the occulter moves towards FM1). (2) Removing the Lyot Stop, scan the occulter along the *x*-axis (positive T_x moves the occulter towards the dark-hole), and find $T_x = T_{x0}$ at which the two symmetric side-lobes of the measured point-spread function (PSF) have the same intensity values. (3) Move the occulter from $T_x = T_{x0}$ -2μm to $T_x = T_{x0}$ +2μm in an increment of ΔT_x=1μm, and record the I_b values. (4) Repeat Steps 1-3 for T_z =-0.1, 0, 0.1, and 0.2mm. (5) Plot the change in I_b , or $I_b(T_x) - I_b(T_{x0})$, as a function of T_x - T_{x0}. The experimental result is shown in Fig. 13(a), and the one predicted by the model is shown in Fig. 13(b). Figure 13(c) shows an example of measured normalized intensity map. There are uncertainties and difference between the measurement and the simulation at least in the following several areas: (1) A monochromatic beam with λ = 808nm was used in the experiment, but the simulation was carried out with λ = 800nm. (2) Both the magnitudes and the registration of the surface error maps used in the simulation are different from what the propagating beam sees on the testbed. (3) The simulation uses the designed OD and phase profiles of the occulter, and they can be different on the testbed. (4) WFC was carried out over a rectangular area in the experiment, but on a D-shaped region in the simulation. (5) The darkness of the dark-hole achieved for the nominal case on the testbed and in the simulation is different. As we can see from Fig. 13(a-b), the measured and the predicted sensitivities are comparable even under the above-mentioned uncertainties and difference between the measurement and the simulation. Although not presented here, we found that the contrast sensitivity to the occulter's lateral and axial motions varies with, among other things, the darkness of the dark-hole achieved for the nominal case, just like in the case of FM1 *x*-motion.

4. CONCLUSION

One of the important milestones of the TPF Coronagraph project is to demonstrate the ability to predict the performance sensitivities of the system at levels consistent with exoplanet detection requirement. In order to gain some general understanding about the potentials and the limitations of the current single-DM HCIT system, we have examined through modeling and simulations the effects of some common errors on the estimation and the EFC-based control of the e-field over a half dark-hole region. Considered cases include two or three dead actuators, lateral and longitudinal movement of the occulting mask, and the lateral movement of a flat optical surface. We have shown that, when two or three actuators die at a time, one of the following four things can happen: (1) The e-field estimation and control algorithms work as usual; (2) the two algorithms become less efficient, but ultimately yield the same level of contrast as obtained when there is no any dead actuator; (3) both the efficiency of the algorithms and the ultimate contrast level get reduced; (4) the algorithms fail completely. The locations of the dead actuators determine which of the above four situations will occur, and we have identified through modeling and simulations some actuators that play crucial role in the e-field estimation and control processes on the HCIT. We have also shown that the lateral movement of a flat optic after WFC degrades the contrast slightly differently in the positive and the negative (towards or away from the dark-hole) directions, and the level of such degradation is strongly dependent on the darkness of the dark-hole achieved before introducing an error to the position of an optical component. The same is true for the de-centering and the defocus of the occulting mask. For this latter case, we compared the model predictions with the experimental results and obtained reasonable agreement between the two.

This work was carried out at the Jet Propulsion Laboratory, California Institute of Technology, under contract with the National Aeronautics and Space Administration.

REFERENCES

1. John T. Trauger, Chris Burrows, Brian Gordon, Joseph J. Green, Andrew E. Lowman, Dwight Moody, Albert F. Niessner, Fang Shi, and Daniel Wilson, “Coronagraph contrast demonstrations with the high-contrast imaging testbed,” Proc. SPIE, **5487**, 1330, 2004.
2. Andrew E. Lowman, John T. Trauger, Brian Gordon, Joseph J. Green, Dwight Moody, Albert F. Niessner, and Fang Shi, “High-contrast imaging testbed for the Terrestrial Planet Finder coronagraph,” Proc. SPIE, **5487**, 1246, 2004.
3. Erkin Sidick, Fang Shi, Scott Basinger, Dwight Moody, Andrew E. Lowman, Andreas C. Kuhnert, and John T. Trauger, “Performance of TPF’s High-Contrast Imaging Testbed: Modeling and simulations, ”Proc. SPIE, **6265**, 62653L, 2006.
4. Amir Give’on *et al*, “Broadband wavefront correction algorithm for high-contrast imaging system,” Proc. SPIE, **6691**, 66910A (2007).
5. *Modeling and Analysis for Controlled Optical Systems User’s Manual*, Jet Propulsion Laboratory, California Institute of Technology, Pasadena, CA.
6. Kunjithapatham Balasubramanian, Daniel W. Wilson, Brian D. Kern, Erkin Sidick, "Thickness-dependent optical properties of metals and alloys applicable to TPF coronagraph image masks," Proc. SPIE vol. 6693, pp. 66930Z, Aug. 2007..
7. Erkin Sidick and Kunjithapatham Balasubramanian, "Effects of optical-density and phase dispersion of an imperfect band-limited occulting mask on the broadband performance of a TPF coronagraph," *Proc. SPIE* vol. 6693, pp. 66931C, Aug. 2007..
8. Erkin Sidick, "Requirements on optical-density and phase dispersion of imperfect band-limited occulting masks in a broadband coronagraph,” *Applied Optics,* vol. 26, pp. 7485-7493, Oct. 20, 2007.
9. Erkin Sidick, Scott A. Basinger, and David C. Redding, “An improved wavefront control algorithm for large space telescopes,” Proc. SPIE, **7015**, 70154P (2008).
10. E. Sidick, S. Shaklan, A. Give’on, and B. Kern, "Studies of the effects of actuator errors on the HCIT/PIAA contrast performance ,” *Proc. SPIE,* vol. 7731, pp.7731-4T, June 2010.
11. Erkin Sidick, " Power spectral density specification and analysis of large optical surfaces ,” *Proc. SPIE*, vol. 7390, pp. 73900L, June 2009.